DE GRUYTER Adv. Opt. Techn. 2022; 11(3–4): 117–135

Review Article

Stefan Zollner*, Farzin Abadizaman, Carola Emminger and Nuwanjula Samarasingha

Spectroscopic ellipsometry from 10 to 700 K

https://doi.org/10.1515/aot-2022-0016
Received April 18, 2022; accepted May 13, 2022;

Abstract: The temperature dependence of the optical constants of materials (refractive index, absorption and extinction coefficients, and dielectric function) can be determined with spectroscopic ellipsometry over a broad range of temperatures and photon energies or wavelengths. Such results have practical value, for example for applications of optical materials at cryogenic or elevated temperatures. The temperature dependence of optical gaps and their broadenings also provides insight into the scattering of electrons and holes with other quasiparticles, such as phonons or magnons. This review presents a detailed discussion of the experimental considerations for temperature-dependent ellipsometry and selected results for insulators, semiconductors, and metals in the infrared to ultraviolet spectral regions.

Keywords: cryostat; dielectric function; electron-phonon interaction; spectroscopic ellipsometry; temperature; windows.

1 Introduction

Spectroscopic ellipsometry [1–3] is an optical reflection technique based on the polarization of electromagnetic waves. It is most commonly used to determine the thicknesses of transparent thin layers on thick single-side polished substrates (such as SiO_2 on Si) in research and development labs or for manufacturing control, for example in semiconductor wafer manufacturing [4] or in the deposition of optical coatings. Ellipsometry can also measure the refractive index of transparent bulk materials with moderate accuracy or determine the real and imaginary parts of the complex refractive index (including the absorption and extinction coefficients) of highly absorbing bulk materials with an absorption coefficient larger than about 1000 cm^{-1}. Depending on the complexity of an optical layer stack, it may also be possible to determine optical constants and thicknesses of thin layers [3].

Beyond these technology applications, spectroscopic ellipsometry is also a materials science tool for the study of materials and their energy spectra. Let's assume for the moment that our material is described by a Hamiltonian H_0 with many eigenstates of **non-interacting** energy levels. Some of these occupied energy levels can interact with light by absorbing a photon, which results in an excited state. Such energy levels form the initial and final states of **allowed transitions** with energy E_j^0, which we call **oscillators**. They result in peaks or other structures in the dielectric function $\epsilon(\omega)$, where ω is the angular frequency. Other occupied energy levels cannot absorb a photon. They are related to **forbidden transitions**. For example, infrared-active phonons can absorb infrared photons, while Raman-active or silent phonons cannot.

For many materials the oscillators E_j^0 can be separated into three groups [5, 6]: (1) Oscillators with $E_j^0 = 0$ result from the absorption of light by free electrons and holes (if any). This is the **Drude response** of metals and doped semiconductors. (2) **Lattice absorption** in insulators and semiconductors occurs in the far- and mid-infrared spectral region up to about 1500 cm^{-1} or 186 meV. (3) **Electronic transitions** usually have energies of 500 meV or higher. They can be observed in the near-infrared, visible, and ultraviolet spectral regions. Therefore, many materials have a region between 200 and 500 meV, where $\epsilon(\omega)$ is real and nearly constant. The value of $\epsilon(\omega)$ in this region is called the high-frequency dielectric constant ϵ_∞. (We should note that some materials like InSb or α-tin have very small band gaps and therefore this spectral separation of oscillators may not always be possible). With this classification of oscillators in mind, we can separate the dielectric function into three terms [7]

$$\epsilon(\omega) = \epsilon_\text{D}(\omega) + \epsilon_\text{L}(\omega) + \epsilon_\text{e}(\omega) \tag{1}$$

representing the Drude, lattice, and electronic absorption.

***Corresponding author: Stefan Zollner**, Department of Physics, New Mexico State University, Las Cruces, NM, USA,
E-mail: zollner@nmsu.edu. https://orcid.org/0000-0001-7752-7941
Farzin Abadizaman, Carola Emminger and Nuwanjula Samarasingha, Department of Physics, New Mexico State University, Las Cruces, NM, USA, E-mail: abadizaman@physics.muni.cz (F. Abadizaman), carola.emminger@uni-leipzig.de (C. Emminger), nuwanjula-s@novami.com (N. Samarasingha)

So far, we have assumed that the oscillators E_j^0 are noninteracting. They arise from the eigenstates of the unperturbed Hamiltonian H_0, which is independent of temperature. The oscillators at E_j^0 are therefore δ-functions with a very small linewidth. We now turn on the interactions between the energy levels or with other quasiparticles and assume that they can be described by an interaction Hamiltonian $H'(T)$. The complete Hamiltonian is therefore [8]

$$H(T) = H_0 + H'(T). \tag{2}$$

For example, the resistivity of a metal is limited by scattering of electrons with the lattice. Similar electron–phonon interactions broaden the final and/or initial states of electronic transitions. Another interaction is the anharmonic decay of optical phonons into acoustic phonons. Equation (2) is therefore the **principal motivation for temperature-dependent ellipsometry**. As we vary the temperature, we can study the eigenstates associated with the perturbed Hamiltonian $H(T)$. By combining measurements over a broad temperature range, we can subtract the effects of the perturbation $H'(T)$ and determine the energy levels of the unperturbed Hamiltonian H_0, for example for comparison with *ab initio* lattice dynamics or band structure calculations. Additionally, the variations of the energy levels with temperature provide information about the nature of the interactions of electrons and holes with other elementary excitations such as phonons, magnons, etc.

The temperature-dependent interaction Hamiltonian $H'(T)$ adds a complex self-energy $\Sigma(T)$ to the unperturbed oscillator energies E_j^0. The oscillator energies observed in the experimental dielectric functions are therefore [8]

$$E_j(T) = E_j^0 + \mathrm{Re}[\Sigma(T)] + \mathrm{Im}[\Sigma(T)]. \tag{3}$$

The real part $\mathrm{Re}[\Sigma(T)]$ is often (but not always) negative and usually leads to a redshift of oscillators with increasing temperature. The imaginary part $\mathrm{Im}[\Sigma(T)]$ is always positive and equals the homogeneous Lorentzian lifetime broadening of an oscillator. (For purposes of this review, we restrict ourselves to highly crystalline materials and ignore the inhomogeneous broadenings often found, for example due to impurities, extended defects, grain boundaries, variations of composition, etc.).

The self-energy $\Sigma(T)$ does not vanish at low temperatures. For example, due to the zero-point energy of a quantum mechanical oscillator, the amplitudes of lattice vibrations do not vanish at $T = 0$. Therefore, we expect to find a red-shift and a broadening of transitions even at very low temperatures. There may also be temperature-independent self-energy contributions, for example due to alloy scattering in random alloys such as Si–Ge solid solutions. Nevertheless, low-temperature measurements usually yield the sharpest peaks with the smallest broadenings. This can help resolve closely spaced oscillators.

The self-energy $\Sigma(T)$ usually varies quadratically at low temperatures and then changes linearly at higher temperatures. Therefore, much information can be gained from measurements between 80 and 700 K, if liquid helium is not available for experiments. Measurements above room temperature up to 700 K or higher are very important to understand the origin of $\Sigma(T)$.

In our discussion of Eqs. (2) and (3), we have neglected that the unperturbed eigenstates E_j^0 of H_0 depend on the lattice constant and therefore also show temperature dependence due to thermal expansion (TE). For optical phonons, this temperature dependence due to thermal expansion is given by [9]

$$\Delta E_j^{\mathrm{TE}}(T) = -3\gamma E_j^0 \int_0^T \alpha_l(\theta)\,\mathrm{d}\theta, \tag{4}$$

where E_j^0 is the unperturbed energy at $T = 0$, $\Delta E_j^{\mathrm{TE}}(T)$ the shift of this eigenstate due to thermal expansion, $\alpha_l(T)$ the linear coefficient of thermal expansion (which depends on temperature), and γ the Grüneisen parameter of this phonon mode. A similar expression applies to the thermal expansion contribution to the shifts of band gaps, which involves the product of the bulk modulus and the pressure dependence of the band gap at constant temperature instead of the Grüneisen parameter [10]. The shift due to thermal expansion in Eq. (4) is usually smaller than the real part of the self-energy $\Sigma(T)$.

2 Experimental details

2.1 Options for heating and cooling

In practice, we have encountered three different experimental setups to vary the temperature of a sample during an ellipsometry measurement.

First, one can place the sample on a hot plate in an ambient environment. This does not allow cooling of the sample, since water will condense on its surface once its temperature falls below the dew point of the ambient. Heating of the sample up to about 100 °C can easily be achieved. For our measurements on metals and semiconductors, we have not found this technique suitable, since our samples usually react with ambient air when heated and form native or thermal oxide layers. For other types of materials, for example oxides, this technique may be useful if only a narrow temperature range is required. This technique is very simple and does not require windows, which limit the spectral range of the measurement or alter the polarization of the incident or reflected light.

The second method uses a sample chamber similar to one available from Linkam Scientific Instruments [11] for heating and cooling. With liquid nitrogen, one can reach temperatures as low as −70 °C. High temperatures up to 600 °C are achievable with resistive heating of the sample combined with water cooling of the chamber.

This chamber can be evacuated or purged with an inert gas such as nitrogen. For our metal or semiconductor samples, this chamber did not prevent reactions with the ambient or residual oxygen in the evacuated chamber, but it may be appropriate for other applications. A similar nitrogen-purged chamber [12] was used successfully to determine the dielectric function of Si from 2.0 to 4.3 eV, the infrared refractive index, and the E_1 critical point energy between 300 K and 1200 K. The oxide thickness rose during heating to a maximum of about 14 nm at 1150 K, which had to be considered when modeling the ellipsometric angles to find the dielectric function. This chamber requires entrance and exit windows. They have a limited range of transparency, which limits the spectral range of the ellipsometry measurement. They also partially reflect the beam (intensity loss) and modify the polarization state of the incident and reflected beams. This must be corrected during data acquisition and analysis, see Section 2.5.

The third method uses an ultrahigh vacuum chamber for heating and cooling, as described in Section 2.2.

2.2 Ultrahigh vacuum chamber design for heating and cooling

Many researchers have realized that only an ultrahigh vacuum (UHV) chamber can consistently protect samples from condensation at low temperatures and oxidation at high temperatures. A typical example is given in Figure 1, which shows a Lakeshore Janis ST-400 cryostat mounted on a J. A. Woollam Co. vertical variable angle of incidence spectroscopic ellipsometer (VASE). The bottomless exterior stainless steel vacuum envelope has four windows mounted at about 0° and 180° for transmission measurements and at about ±70° for reflection and ellipsometry measurements. The windows are misaligned slightly to avoid multiple reflections. To achieve good vacuum base pressure (as low as 10^{-8} Torr at room temperature), the vacuum envelope is mounted directly on top of a small air-cooled turbopump (Agilent TwisTorr 84 FS), which is backed by a roughing pump. The whole assembly is attached to the Woollam VASE instrument, just like other sample stages. The same assembly (with different windows) can also be attached to a Woollam Fourier-transform infrared (FTIR) VASE instrument. With some modifications, cryostat measurements are also possible in the nitrogen-purged vacuum ultraviolet (VUV) VASE instrument [13–15]. Below 80 K, the pressure usually falls below 10^{-8} Torr, since the sample holder acts as a cryopump. At 800 K, the pressure may rise up to 10^{-6} Torr or even higher, as the sample outgases. Care must be taken not to let the pressure rise too much. A high pressure when heating the sample indicates that the sample may disintegrate. This may lead to thin layers being deposited on the inside of the vacuum windows, which reduces their transparency and may also disturb the polarization. The vacuum shroud contains an electrical UHV feedthrough to measure the sample temperature with a thermocouple, Si diode, or Pt resistor.

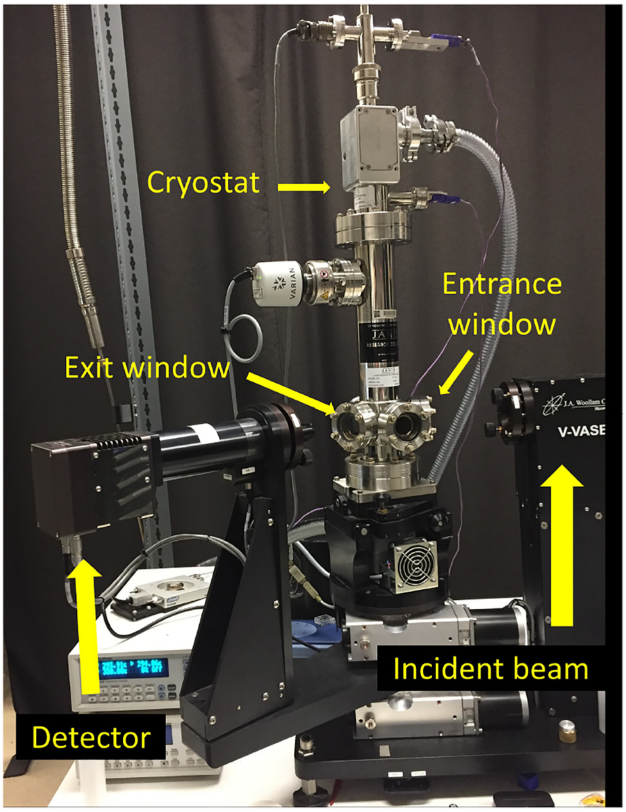

Figure 1: The Lakeshore Janis ST-400 ultrahigh vacuum cryostat is shown attached to a J. A. Woollam Co. vertical variable angle of incidence spectroscopic ellipsometer (VASE).

Inside the vacuum shroud rests a cold finger insert made from copper with high thermal conductivity. It contains a cryogen reservoir, which is filled with liquid helium or nitrogen for cooling. The top of the insert is heated to prevent the UHV seal between the insert and the stainless steel vacuum shroud from freezing (which may cause vacuum leaks). Sample temperatures near 10 K can be achieved with helium and about 80 K with nitrogen. The evaporating cryogen can be captured at the vent port or allowed to escape into the ambient. The cryogen is usually supplied from a Dewar through an evacuated transfer arm. If a recirculating helium cooler is used instead, one has to worry about vibrations being transferred to the optical setup, which may increase the noise in the ellipsometry measurement. This will require some testing and perhaps isolation measures.

Heating of the sample is achieved with a 50 Ω resistor located just under the cryogen reservoir. To reduce corrosion of the cold finger insert at high temperatures, the vent port must be evacuated with a roughing pump while the cryogen intake is plugged with a rubber stopper. Even with this precaution, corrosion is not avoidable in the long run. The heater or thermocouple may fail or vacuum leaks may develop. The cold finger should therefore be treated as a consumable, unfortunately, for measurements at the highest temperatures. Additional details, photos, and drawings can be found at the manufacturer’s web site [16].

2.3 Mounting of samples

Below the cryogen reservoir, a two-inch long semicylindrical copper sample holder with a one-inch diameter is attached. Slotted through-holes allow a slight shift of the sample holder along the surface normal to accommodate different sample thicknesses. How to mount the sample on this sample holder deserves some discussion, especially for small samples. The sample must have good thermal contact with the sample holder to establish thermal equilibrium. This requirement suggests the use of a paste based on silver or carbon nanoparticles. However, this paste may outgas at higher temperature and may get redeposited on the windows, which is detrimental, or on other surfaces. Furthermore, it is important (especially for infrared measurements, where the copper sample holder has a high reflectivity) that the ellipsometry beam only hits the sample, not the sample holder. If light reflected by the sample holder hits the detector, then the ellipsometry measurements yield false results. Usually, this can be recognized by a higher than normal depolarization signal. To avoid such sample holder reflections, one may cover the exposed sample holder (areas not covered by the sample) with a silver or carbon-based paint, which scatters the light rather than reflecting it. Again, this paste may outgas at high temperatures. It is even better to have multiple sample holders available, to match the width of the sample with that of the sample holder. The highly reflective copper sample holder may also increase the backside reflections of transparent samples. Their back side will have to be roughened even more than for measurements of samples in ambient at room temperature on less reflective sample holders.

For our purposes and for sufficiently large and mechanically stable samples, we found it best to mount the sample mechanically (without any paste) with horizontal stainless steel strips that push the sample against the sample holder, see Figure 2. The sample should have the full width of the sample holder and the beam should not hit the stainless steel strips, unless they are sufficiently rough or covered with a nonreflective paste. The steel strips are attached to the sample holder with spring-loaded screws. Different sample heights can be accommodated by a copper sample holder with several pairs of screw holes. To achieve the best vacuum, the screw holes should go through the entire sample holder. If that is not feasible, then vented screws must be used.

Mounting the sample in the correct position can be tricky, especially for small samples. It is better not to seal the cryostat until the correct position of the sample has been verified with a test measurement. Given all these considerations, the ideal sample size for commercial instrumentation is probably about 20 by 20 mm^2; the smallest sample size is about 10 by 10 mm^2. It is easier to measure small samples on the VASE because it can be seen clearly where the white light beam hits the sample. On the FTIR-VASE, the infrared beam is not visible; on the VUV-VASE, there is no optical access to see the beam. In both cases, small samples are harder to measure. Some researchers have built custom sample holders to measure small samples at the expense of intensity.

Figure 2: A Si sample mounted on the copper sample holder with horizontal stainless steel strips.

2.4 Temperature measurement and control

Precise temperature measurements require different sensors based on the desired temperature range. Only a Si diode thermometer provides precise results at the lowest temperatures in our Janis cryostat, but such diodes are rather large and are rated only up to 500 K. These diodes are suitable for mounting near the cryogen reservoir or behind the sample holder, but they cannot usually be mounted in a way to provide the precise temperature of the sample surface. Fortunately, the thermal conductivity of many materials is high at low temperatures and therefore the temperature difference between the cryogen reservoir and the sample surface is usually quite small.

For temperature measurements between 80 and 800 K, we use two type E (NiCr–CuNi) thermocouples. One of them is mounted near the cryogen reservoir, while the other one is placed between the steel mounting strip and the sample surface. The latter provides an accurate temperature reading of the sample surface. The difference between the temperatures measured by the two sensors can be as high as 50 K due to the reduced thermal conductivity of copper at the highest temperatures.

To achieve the lowest possible sample temperatures (estimated to be about 10 K with helium cooling and 80 K with nitrogen cooling), the sample and sample holder are enclosed by a cylindrical gold-plated copper radiation shield, which has holes for the incident and reflected beam. This heat shield also reduces the temperature gradient between the heater and the sample surface at the highest temperatures and is therefore indispensable, despite the corrosion expected from repeated use at 800 K.

The electrical signals from both types of temperature sensors are read by a Lakeshore 300-series temperature controller, see Figure 1. The same controller also provides the power applied to the heater to achieve the temperature setpoint based on a proportional-integral-differential (PID) algorithm. The controller can either be programmed manually or it can be connected to the ellipsometry data acquisition program with a computer interface.

The temperature dependence of band gaps is typically in the range of 0.1–1 meV/K. Critical point energies can be measured with a precision that is not usually better than 1 meV. Therefore, the temperature should be held stable to within 1–10 K. That is not usually an issue with modern PID temperature controllers.

2.5 Windows for different spectral ranges

The windows of the cryostat must meet several criteria: (1) They must be transparent over the spectral range of interest. (2) They should have a low refractive index to minimize reflection losses. (3) They must be mechanically stable and provide a good vacuum seal. (4) They should have a small (or at least a predictable) impact on the polarization of the incident and reflected beams. For the near-infrared to quartz-ultraviolet spectral range (190–2500 nm), quartz (fused silica) is the window material of choice. Its refractive index is on the order of 1.5, which leads to reflection losses (from both windows) of only about 15%. Depending on the type of quartz, transmission can be optimized for the ultraviolet or near-infrared spectral region. Excellent transitions from quartz to stainless steel or molybdenum with low leakage rates can be achieved. Strain-free UHV quartz windows are available commercially [17, 18]. On the other hand, commercial ellipsometers usually have the ability to correct the influence of the windows on the incident and reflected polarization states with a proprietary algorithm, which allows a simpler window design than the Bomco windows. Abadizaman has summarized the available open literature on this topic in an appendix of his Ph. D. thesis [19]. Even at the highest sample temperatures, there is no significant rise of the window temperature. Therefore, we are not concerned about the temperature dependence of the polarization effect due to windows. In the vacuum ultraviolet spectral region (135–1700 nm), CaF_2 with its band gap near 10–12 eV is chosen most often as a window material. It has a refractive index of about 2 at 10 eV, leading to moderate reflection losses.

In the mid- and far-infrared spectral regions, quartz is highly absorbing and cannot be used as a window material. The infrared ST-400 cryostat ships with ZnSe windows, which limit the upper wavelength range to about 16–22 μm. We replaced these ZnSe standard viewports with commercial diamond windows produced by chemical vapor deposition and mounted on a UHV flange [20]. These diamond windows are expensive and the high refractive index near 2.4 leads to reflection losses of over 50%. On the other hand, they are completely transparent from the Terahertz range to the deep ultraviolet, limited by the diamond band gap of 5.47 eV, and allow good UHV seals with stainless steel flanges.

Another common infrared window material is thallium bromoiodide (KRS-5). These thallium compounds are highly toxic. They are insoluble in water and not hygroscopic, but they will deteriorate over time due to poor mechanical stability and are difficult to polish flat. The KRS-5 refractive index is also near 2.4 and therefore the reflection losses will be just as large as with diamond, making cost the only advantage of KRS-5. Windows on UHV flanges are available commercially [21].

A third mid-infrared option comprises the class of alkali halide compounds, including NaCl ($n = 1.53$), KBr ($n_\infty = 1.55$), KCl ($n_\infty = 1.48$), CsI ($n_\infty = 1.78$), and RbI ($n_\infty = 1.64$). These salts have the advantage of a lower refractive index (resulting in reduced reflection losses), but they are generally water soluble and hygroscopic, which requires a well-controlled low-humidity lab atmosphere. AgCl and AgBr are also good choices, but they are more expensive. In general, a larger reduced mass of the compounds leads to lower infrared-active phonon energies, which increases the range of transparency. Of all these options, KBr is the most widely used [22–24]. With proper climate controls, KBr windows can last for years.

The polar materials mentioned so far all absorb light in the far-infrared spectral region, where only nonpolar crystals like diamond (already mentioned) are transparent. A more traditional option is Mylar. A 6–20 μm thick Mylar film has a broad transparency range, but the thickness must be selected carefully to avoid interference fringes. Mylar is also anisotropic and therefore window corrections are crucial [25]. Unfortunately, Mylar is very fragile and can be easily torn in a high pressure gradient. If rubber o-rings are used to secure the thin Mylar foil on the window flange, then UHV is not achievable. In one experimental setup [26], the whole far-infrared ellipsometer, including the sample chamber, is pumped down to a pressure below 1 mbar and then the sample chamber is pumped down to 10^{-6} mbar. This reduces the pressure differential the Mylar foil is exposed to and still achieves a high vacuum inside the sample chamber. This setup [26] is particularly suitable for far-infrared ellipsometry at an infared synchrotron beamline.

Measurements over a broad spectral range (for example from 0.1 to 6.0 eV) may require the use of more than one instrument (FTIR-VASE and VASE in this case). This may lead to a small mismatch of the data in the region where both instrument ranges overlap due to uncertainties of the window parameters. Abadizaman [19] has described a technique to match the data sets by adjusting the window parameters in the infrared spectral region.

2.6 Black-body radiation

At elevated temperatures, the sample holder and the gold-plated heat shield can produce significant amounts of black-body radiation. Modern ellipsometers measure the reflected intensity for each configuration of the polarizing elements with and without the incident light hitting the sample, either by employing a shutter or by chopping the incident beam. This allows to subtract the dark currents in the detection system and intensity from spurious light sources, such as ambient room light or black-body radiation, but only within the linearity limits of the detector and the associated electronics. At the highest temperatures, the black-body radiation can saturate the detector used in ellipsometry experiments. This is true particularly for near-infrared VASE measurements using an InGaAs detector. A Si photodiode or a photomultiplier (used at larger photon energies) have a larger range of linearity and are affected less than the InGaAs detector at lower energies (where black-body radiation is stronger). It may also be possible to use customized detection electronics, targeted to allow a higher total light intensity without saturating the circuit by reducing the overall amplification factor of the circuit. Using a photomultiplier tube, ellipsometry measurements of Si between 2.0 and 4.3 eV up to 1200 K have been reported [12].

The effect of black-body radiation is shown in Figure 3 based on work described in the supplementary material of ref. [27]. For high-

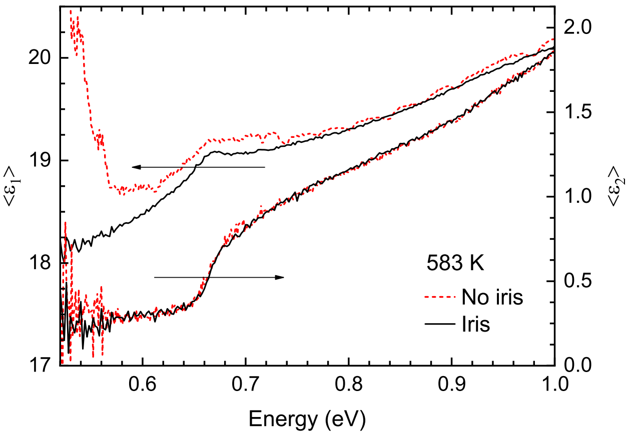

Figure 3: Pseudodielectric function of Ge at 583 K from 0.5 to 1.0 eV with and without an aperture (iris) placed between the sample and the detector to reduce the effects of black-body radiation. Data from ref. [27].

temperature VASE measurements, we therefore place a small carefully aligned aperture just outside the exit window of the cryostat. The aperture is just larger than the reflected beam and therefore reduces the overall black-body radiation. This procedure was not needed for FTIR-VASE measurements at high temperature [28].

2.7 Surface effects in UHV during heating and cooling

For precise ellipsometry measurements on bulk materials, surface layers (including surface roughness, native oxides, and adsorbed overlayers such as water) must be minimized as much as possible. This can be achieved with *ex situ* as well as *in situ* techniques. Wet cleaning techniques have been described for many semiconductors to reduce the native oxide thickness while keeping the sample in a flow of dry nitrogen gas during the ellipsometry measurement [29]. For oxides, a wet clean using organic solvents followed by UV ozone clean can be used [30, 31]. This UV ozone clean is also effective to remove water from metal surfaces [32]. For bulk Ge and Ge–Sn alloys, we developed a hybrid technique involving a wet ultrasonic clean in isopropanol and water followed by UV ozone clean [27]. The effectiveness of each clean is confirmed with an ellipsometry measurement before mounting the sample in the cryostat for temperature-dependent measurements. The cleanest surface will have the lowest/highest value of the ellipsometric angle Δ (for an incidence angle lower/larger than the Brewster angle) below the band gap (for semiconductors and insulators) and the highest value of $\langle\epsilon_2\rangle$ at the E_2 critical point (for semiconductors) [29, 33]. For insulators, the cryostat windows and surface overlayers both affect primarily the ellipsometric angle Δ. Therefore, it can be difficult to distinguish between window and surface effects in a measurement.

After the best possible *ex situ* preclean for the material, the sample is immediately loaded in the UHV chamber, but the pumps are not turned on yet. An ellipsometry measurement (with air still in the cryostat) should yield the same pseudodielectric function as the measurement just before the sample was loaded in the cryostat. If the results are different and cannot be explained with a gradual growth of surface overlayers, then this indicates an issue with the parameters describing the window effects. The window calibration may have to be repeated using a SiO_2 on Si calibration sample. After this control measurement, the pumps are turned on. It will take about 24 h until the base pressure of 10^{-8} Torr is reached. In most cases, the sample is then heated to 800 K overnight to outgas any residual adsorbed surface layers, followed by a cooldown of the sample to room temperature and another control measurement.

An example of this process for bulk GaP is shown in Figure 4 from the supplemental material in ref. [28]. We report the surface layer thickness in our experiments, modeled as a 50/50 mixture of GaP and voids within the Bruggeman effective medium approximation. We call this the *apparent* surface layer thickness, because it might be affected by systematic errors from the cryostat windows. An initial measurement of the GaP sample in air (without windows) finds a surface layer thickness of 38 Å, shown by the green data point. The sample is then mounted in the cryostat followed by pumping to UHV conditions. This reduces the surface layer thickness to 29 Å, as shown by the blue data point. This reduction might be due evaporation of some of the overlayer, but it could also be due to errors caused by our windows. We then heat the sample to 800 K for several hours and let it cool down to room temperature overnight. This reduces the surface layer thickness to 9 Å, as shown by the red data point. Most likely, this value of 9 Å represents the residual surface roughness, after all adsorbed contaminants have evaporated. We now start our temperature series at 80 K, where the surface layer thickness is 19 Å. We gradually increase the temperature to 275 K and measure the pseudo-dielectric function at each step for several hours. This increases the surface layer thickness to 48 Å, as ice forms on the sample. At the next temperature (300 K), the surface layer thickness is only 18 Å, because most of the ice has evaporated. As we heat the sample to 325 K, the surface layer thickness is 8 Å and it gradually is reduced to zero as we heat towards 700 K. It is not likely that the surface layer thickness will actually vanish at 700 K. It is more likely that our data are affected by experimental errors due to the diamond windows. These windows are not getting warm, even at the highest sample temperatures. Therefore, the errors due to the windows are likely independent of temperature. It is likely that we underestimate the surface layer thickness in the cryostat by about 10 Å, due to the retardance of the diamond windows. This discussion emphasizes that one must be careful when interpreting changes of optical constants with temperature. A careful preparation of the sample is required to minimize surface overlayers. It can be very helpful to heat the sample for several hours to reduce airborne molecular contamination, if this does not change the properties of the sample. It is inevitable for ice to form on the sample below room temperature, even under the best (10^{-8} Torr) vacuum conditions achievable in our setup.

A similar discussion of the surface layer thickness during a temperature-dependent ellipsometry measurement for bulk Ge can be found in the supplemental material of ref. [27], see Figure 5. Below room temperature, the apparent native oxide thickness increases gradually as the measurements progress, since ice from the residual pressure in the UHV chamber forms on the sample. Above room temperature, the ice desorbs and the surface layer thickness decreases. Above 500 K, the surface layer increases due to thermal oxidation of Ge [34].

Drastic differences of the pseudodielectric function at room temperature before and after heating in the UHV chamber can also be found for bulk nickel [35, 36]. Since surface overlayers on Ni desorb near the Curie temperature at around 600 K, it is easy to confuse surface effects with changes in the magnetic structure of Ni [36].

Surface oxidation can be even more pronounced in nitrogen-purged ellipsometry chambers at very high temperatures [12].

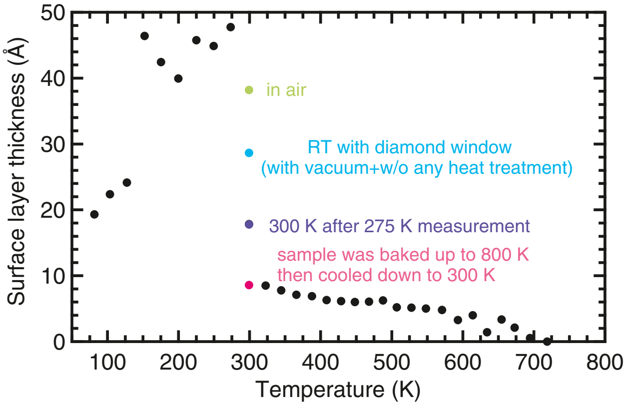

Figure 4: Evolution of the apparent roughness layer thickness on GaP during a temperature-dependent ellipsometry measurement. Data from ref. [28].

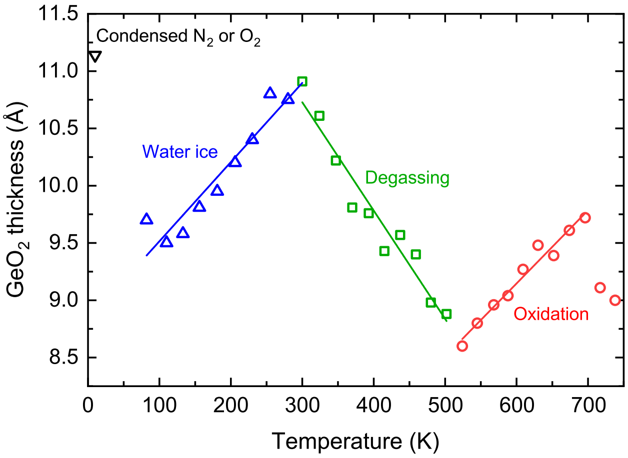

Figure 5: Thickness of the native oxide on Ge as a function of temperature. Data from ref. [27].

2.8 History

Temperature-dependent spectroscopic ellipsometry measurements in a UHV chamber from 0.5 to 6.0 eV and from 77 to 700 K were performed on bulk Ni, Cu, and Au and noble metal alloys as early as 1967 [37–39]. These publications describe the thermal cleaning effect and the need for experimental adjustments to overcome the black-body radiation. The temperature dependence of band gaps and critical points in the dielectric functions of semiconductors was studied systematically by Cardona's group in Stuttgart from the mid-1980s [40–43]. The theory for these shifts and broadenings was developed by Allen and Heine [44] and was reviewed by Cardona and Gopalan [8]. More recent experiments are presented in this review.

3 Temperature dependence of the refractive index of insulators

Ellipsometry is not the most accurate technique to determine the refractive index of bulk transparent materials. Much higher accuracy can be achieved with minimum-deviation prism methods, but such setups are rare [45–47]. Interferometric techniques [48, 49] are also competitive. Nevertheless, ellipsometry offers a convenient method to determine refractive indices over a broad spectral and temperature range.

For insulators and semiconductors without free carriers, the dielectric function in the infrared spectral region can be written as a sum of Lorentzian oscillators [7]

$$\epsilon(\omega) = \epsilon_\infty + \sum_i \frac{A_i\omega_i^2}{\omega_i^2 - \omega^2 - i\gamma_i\omega}, \tag{5}$$

where the sum runs over all infrared-active (transverse optical, TO) phonons with amplitude A_i, angular frequency ω_i and broadening γ_i. The high-frequency dielectric constant introduced earlier can be expressed as [8, 50]

$$\epsilon_\infty = 1 + \left(\frac{E_u}{E_{\mathrm{Penn}}}\right)^2, \tag{6}$$

where E_u is the unscreened plasma frequency of the valence electrons [28] and the Penn gap E_{Penn} represents an average separation of the valence and conduction band. For many semiconductors, E_{Penn} is approximately the same as the energy of the interband critical point E_2 or the band gap at the symmetry point X in the face-centered cubic Brillouin zone.

The temperature dependence of the high-frequency dielectric constant is therefore given as [28, 48]

$$\frac{d\epsilon_\infty}{dT} = -3\alpha_l(\epsilon_\infty - 1) - 2(\epsilon_\infty - 1)\frac{d\ln E_{\mathrm{Penn}}}{dT}. \tag{7}$$

The first term due to volume expansion with the linear thermal expansion coefficient α_l is usually negative. The second term, which describes the pure temperature effect, is usually (but not always) positive, because the Penn gap (E_2 energy) usually decreases with increasing temperature. Both terms are similar in magnitude and cancel partially.

For spinel ($MgAl_2O_4$), a temperature coefficient $d\epsilon_1/dT = 3.2 \times 10^{-5}/K$ was found at 2 eV [51]. A similar value was determined for $LaAlO_3$ [52]. These values are smaller than the thermal expansion term alone (-10^{-4}/K) because of the partial cancellation from the second term. $d\epsilon_1/dT$ may even change its sign [52] because of the temperature dependence of the various parameters in Eq. (7).

The temperature dependence of ϵ_∞ for GaP [28] is shown in Figure 6. At room temperature, the rate of change of ϵ_∞ is about 4.5×10^{-4}/K, which compares favorably with the prediction of 6.4×10^{-4}/K given by Eq. (7). Using the Lyddane–Sachs–Teller relation

$$\epsilon_s = \epsilon_\infty \frac{\omega_{\mathrm{LO}}^2}{\omega_{\mathrm{TO}}^2}, \tag{8}$$

where ω_{TO} and ω_{LO} are the angular frequencies of the transverse and longitudinal optical phonons in a zinc blende crystal, it is also possible to calculate the static dielectric constant ϵ_s from the high-frequency one. This result is also shown in Figure 6. Such results are typical. A similar value of $d\epsilon_\infty/dT = 1.6 \times 10^{-4}$/K for the ordinary optical constants was found for wurtzite ZnO [53]. Note that $d\epsilon/dT = 2n dn/dT$. Other examples for silicon and germanium, where $\epsilon_s = \epsilon_\infty$, are given in Refs. [12, 54].

In low-symmetry monoclinic Ga_2O_3 crystals, the high-frequency dielectric function ϵ_∞ is a tensor with four different elements, including one off-diagonal element. Using Mueller matrix ellipsometry of two Ga_2O_3 single crystals with

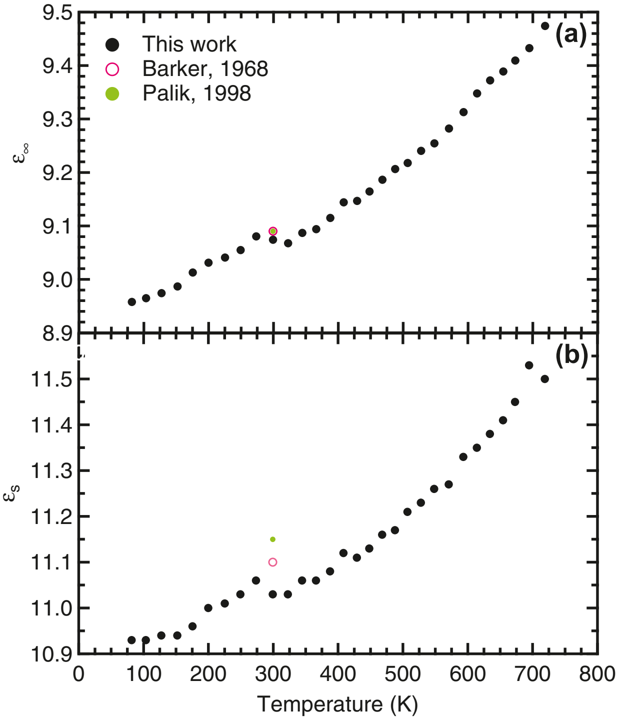

Figure 6: Temperature dependence of the (a) high-frequency and (b) static dielectric constant of GaP. Results from the literature at 300 K are also shown. Reprinted from ref. [28] with the permission of AIP Publishing.

different surface orientations, Mock et al. [55] could determine the temperature dependence of all four tensor elements of ϵ_∞ from extrapolating the dielectric tensor to low frequencies. They also determined the temperature dependence of the energies of six different critical points, which are required to fit the dielectric tensor of Ga_2O_3.

It is rather unusual, if ϵ_1 or the refractive index n **decrease** with increasing temperature, but it is possible due to phase transitions or in the vicinity of interband optical transitions. This occurs, for example, in the mineral delafossite $CuFeO_2$, where ϵ_1 at 1 eV decreases with increasing temperatures below 50 K due to magnetic phase transitions at 11 K and 16 K [56]. More commonly known is the temperature dependence of the static dielectric constant of ceramics such as $BaTiO_3$ used as capacitor materials, where the crystal symmetry is lowered as the temperature decreases [57].

4 Temperature dependence of band gaps and broadenings

The temperature dependence of band gaps and broadenings has been measured for many different semiconductor materials [8]. As an example, we show the dielectric function of germanium near the direct band gap E_0 between 80 and 450 K in Figure 7. Its imaginary part ϵ_2 shows a step-like absorption edge, which is accompanied by a discrete exciton peak at low temperatures and broadened at higher temperatures. The corresponding peak of ϵ_1 is Kramers–Kronig consistent.

For the precise determination of the band gap and broadening at each temperature, one calculates the second derivatives of the spectra with respect to photon energy using sophisticated numerical methods, which remove the nonresonant background from higher-energy interband transitions [27, 54]. These derivatives are then fitted with analytical oscillator lineshapes, for example those introduced by Aspnes [58, 59] for interband critical points with parabolic bands of the form

$$\epsilon(\omega) = B - A\exp(i\phi)(\hbar\omega - E_g + i\Gamma)^{-\mu}, \tag{9}$$

where A, ϕ, E_g, and Γ are the amplitude, phase angle, energy, and Lorentzian broadening of the critical point and B is the nonresonant background from other critical points. $\hbar$ is the reduced Planck's constant. This lineshape does not work well for the direct band gap E_0 of Ge, which cannot be described as a Lorentzian peak ($\mu = 1$) or a square-root onset of absorption for direct transitions ($\mu = -0.5$). Instead, we have used the Elliott–Tanguy oscillator lineshape to describe the dielectric function [54, 60], which includes the excitonic Sommerfeld enhancement of band-to-band transitions. Results are shown by the lines in Figure 7.

The only adjustable parameters to achieve the fits shown in Figure 7 are the energy and broadening of the direct gap (and two Sellmeier parameters for the nonresonant contributions to ϵ_1), because the peak amplitude can be calculated from the momentum matrix element within $\vec{k} \cdot \vec{p}$ theory [54]. Results are shown by symbols in Figure 8. Energies and broadenings vary quadratically at low temperatures and linearly at higher temperatures. Empirically, this is described by a Bose–Einstein model

$$E(T) = E_0 - E_b\left[1 + \frac{2}{e^{\Omega/kT} - 1}\right] \tag{10}$$

and a similar equation for the broadenings [40]. E_0 is the transition energy derived from eigenstates of the unperturbed Hamiltonian H_0 in Eq. (2), which are perturbed through the interaction with another quasiparticle (usually a phonon or magnon) with energy Ω. E_b is the coupling strength and k the Boltzmann constant. The second term in Eq. (10) represents the real part of the complex self-energy Σ introduced in Eq. (3). This model neglects the redshift of band gaps due to thermal expansion of the crystal, which is

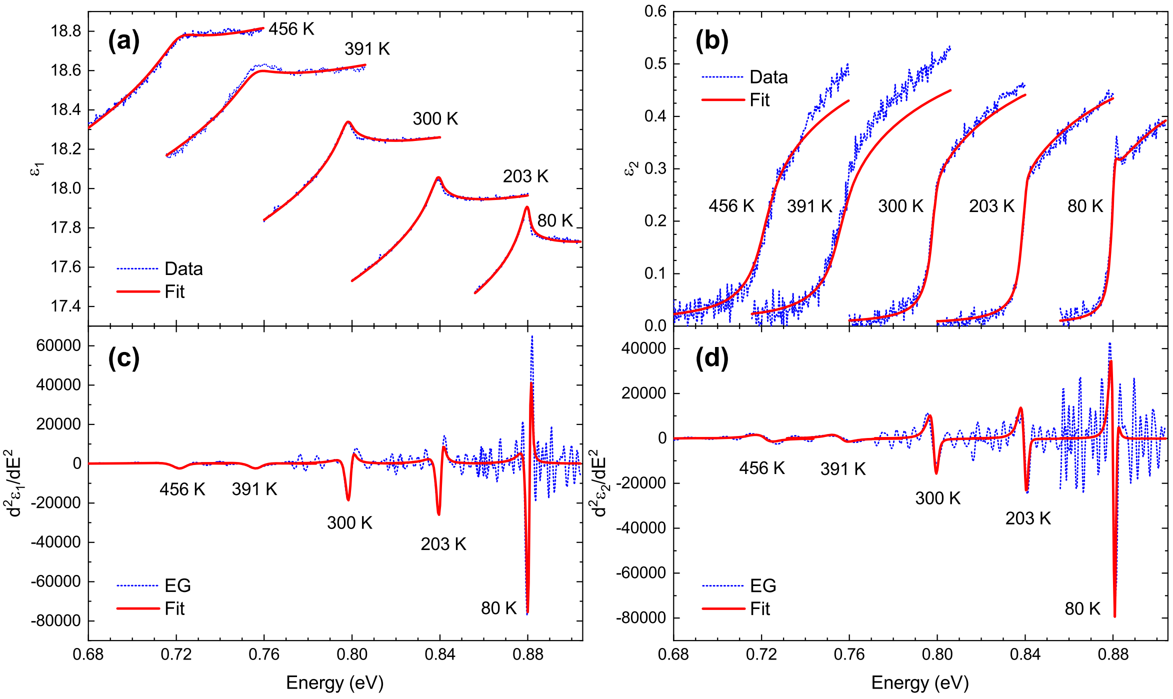

Figure 7: Temperature dependence of the (a) real and (b) imaginary parts of the dielectric function of Ge near the direct band gap E_0 and (c, d) their second derivatives with respect to photon energy calculated using an extended Gaussian (EG) numerical filter. The lines show fits to the data using the Elliott–Tanguy oscillator. Reprinted from ref. [54] with the permission of AIP Publishing.

usually smaller than the scattering shift described by Eq. (10).

As a second example, the dielectric function of Si between 2.0 and 4.3 eV at temperatures up to 1123 K is shown in Figure 9. It is dominated by the critical points E_1 around 3.4 eV and E_2 around 4.2 eV, which can be fitted with Eq. (9) to determine the energies and broadenings. These show a similar behavior as the direct gap of Ge, see Figure 8, and can also be described with a Bose–Einstein model (10).

The precise numerical procedure to fit critical point spectra can have a significant impact on the resulting band gaps and broadenings [61]. For example, fitting the dielectric function or its first, second, or third derivatives can yield different results [12]. Since the excitonic phase angle ϕ and the energy E_g are strongly correlated, it is possible to obtain an invalid temperature dependence of the energy E_g if ϕ is treated as a temperature-dependent parameter [12]. On the other hand, the excitonic phase angle ϕ should depend on temperature, since the excitonic Coulomb force between the electron and the hole decreases with increasing temperature [40]. Experimentally, window effects and surface layers will also impact the fitted phase angle ϕ and therefore can slightly affect the energies. This problem has been solved for the direct band gap of Ge (see Figure 8) where the introduction of temperature-dependent amplitudes and phase angles could be avoided, since the excitonic effects were included explicitly with the Elliott–Tanguy model [54].

The optical spectra of wurtzite compounds like ZnO near the direct band gap are more complicated to fit, because the crystal field splitting and the small spin–orbit splitting result in three excitons with several exciton-phonon replicas. Once these effects are properly taken into account, the temperature dependence of the band gap energy and broadening of wurtzite ZnO [53] resembles the results for Ge shown in Figure 8.

To understand the optical spectra and band structure of wide band-gap materials, ellipsometry measurements in the vacuum-ultraviolet spectral range are required. Results up to 8.5 eV below room temperature have been reported for In_2O_3 [13], Ga_2O_3 [14], and CuI [15]. As shown in Figure 10, CuI shows the typical E_0, E_1, E_0’, and E_2 critical points of a compound semiconductor, but shifted to higher energies. The broadenings and energies of these critical points follow Eq. (10). The excitonic enhancement of the E_0 exciton is quite pronounced at 10 K and decreases at higher temperatures [15].

Interband critical points are observed not only in semiconductors, but also in metals. A recent example is the temperature dependence of the dielectric function of Ni from 77 to 770 K [62]. Within the framework of Eq. (1), the contributions of the free carriers are described with two

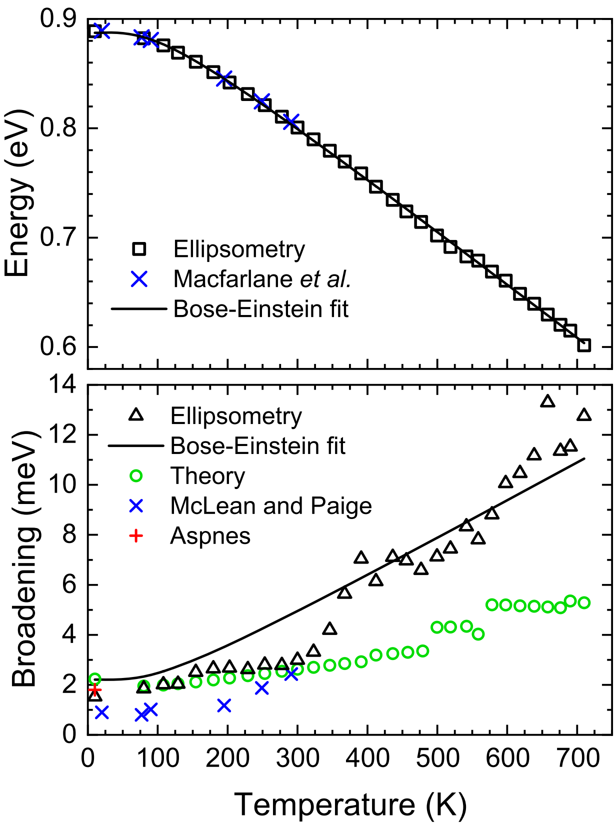

Figure 8: Temperature dependence of the energy and Lorentzian broadening of the direct gap of Ge (symbols) fitted with a Bose–Einstein model given by Eq. (10). See ref. [54] for more details.

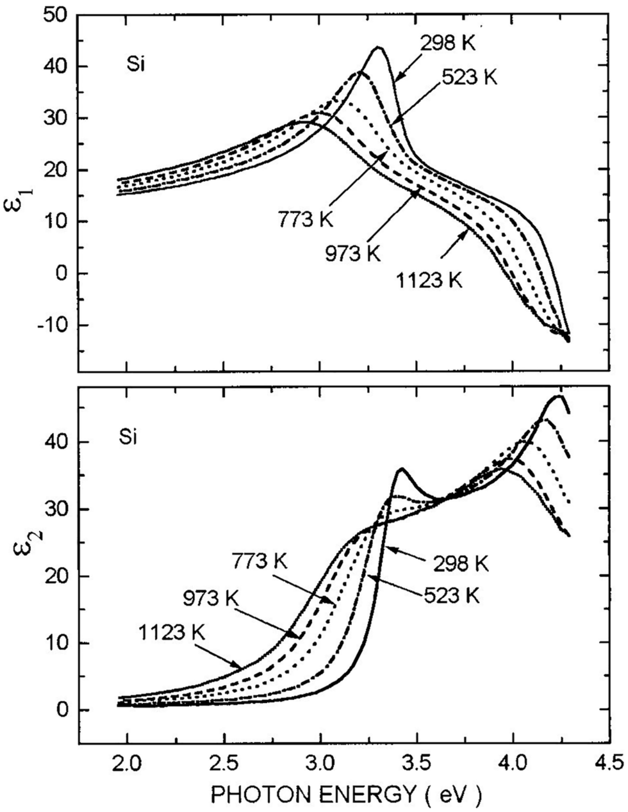

Figure 9: Temperature dependence of the dielectric function of undoped Si from 298 to 1123 K. Reprinted from ref. [12] with the permission of AIP Publishing.

Drude oscillators and interband transitions with four Lorentzians, the strongest one at 4.8 eV. Fitting the temperature dependent redshift of this main peak with Eq. (10) results in a boson energy $\Omega = 53 \pm 3$ meV. This value is larger than optical phonon energies of Ni (below 30 meV), but of the right magnitude for a magnon energy. We therefore conclude that the main absorption peak of Ni at 4.8 eV is strongly perturbed by magnons (quantized spin waves), which lead to a red shift of this peak with increasing temperature.

While the redshift of the main absorption peak of Ni at 4.8 eV with increasing temperature is similar to Si, Ge, and many other semiconductors, the temperature dependence of the broadening of this peak shows a very unusual behavior, see Figure 11. Instead of a gradual increase of the broadening with increasing temperature (as seen in Figure 8 for the direct band gap of Ge) we observe a decrease of the peak width, which seems to follow the normalized magnetization M/M_0 below the Curie temperature T_C and remains constant above T_C. Our interpretation is that the main peak of Ni is a doublet below T_C arising from two bands in the vicinity of the L-point separated by the exchange splitting of the d-band [38], which is on the order of 0.38 eV. The exchange splitting vanishes above T_C and the two peaks merge into a single peak, which reduces the broadening as shown in Figure 11. The temperature dependence of the dielectric function of Ni displays several other interesting phenomena related to its magnetic properties, which are beyond the scope of this review [62].

5 Anharmonic phonon decay

Scattering with other particles (phonons or magnons) by electrons and holes participating in interband transitions affects the dielectric function in the near-infrared to UV spectral range, as discussed in Section 4. Similarly, the lattice absorption in insulators and semiconductors by long-wavelength infrared-active optical phonons also changes with temperature.

We select the wide band-gap semiconductor GaP as an example, see Figure 12. With increasing temperature, the

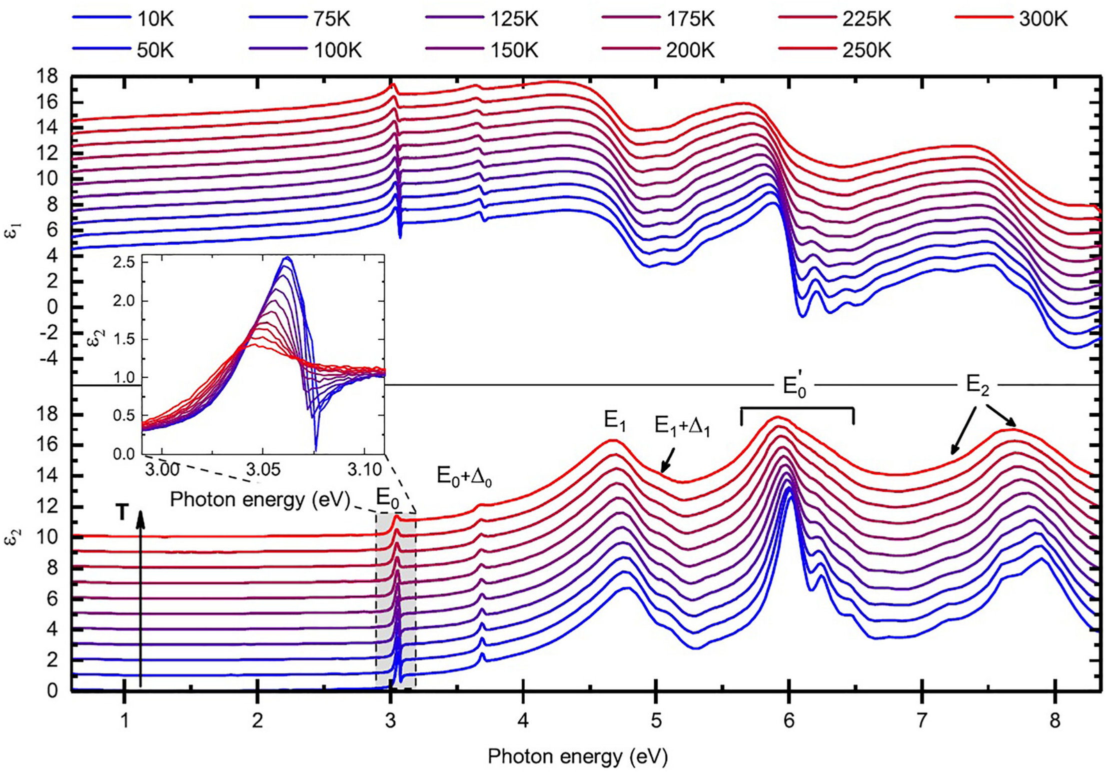

Figure 10: Temperature dependence of the dielectric function of a thin CuI layer on sapphire from 10 to 300 K. The spectra are shifted vertically for clarify. The inset shows ϵ_2 near the excitonic E_0 resonance. Reprinted from ref. [15] with the permission of AIP Publishing.

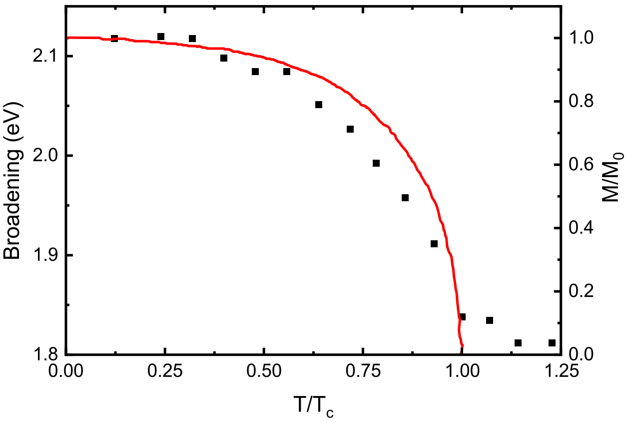

Figure 11: Broadening of the main peak of Ni at 4.8 eV (symbols) and normalized magnetization (line). Data from ref. [62].

transverse optical (TO) phonon peak of ϵ_2 shifts towards lower energies and broadens. The peak amplitude also decreases, because [28]

$$\epsilon_2(\omega_{\mathrm{TO}}) \approx (\epsilon_s - \epsilon_\infty)\frac{\omega_{\mathrm{TO}}}{\gamma_{\mathrm{TO}}}. \tag{11}$$

The infrared dielectric function can be fitted with different oscillator models [7, 28] to determine the phonon parameters. The peak of ϵ_2 occurs at ω_{TO} while the peak of the loss function $-\mathrm{Im}\frac{1}{\epsilon}$ determines ω_{LO}.

The temperature dependence of the TO and LO energies of GaP [28] is shown in Figure 13. Both phonon modes show a distinct redshift with increasing temperature, similar to the redshift of the direct band gap of Ge shown in Figure 8. The thermal expansion contribution to this redshift is small (dashed). The corresponding TO and LO broadenings increase with temperature [28], see Figure 14. Redshifts and broadenings of phonons have been studied for decades with Raman spectroscopy [9], but the use of FTIR ellipsometry for this purpose is new.

The theory of these temperature effects on phonons is complicated [9, 63], but can be summarized as follows: An optical phonon has a finite lifetime on the order of a few 10^{-12} s. Through an anharmonic perturbation of the Hamiltonian H_0 with self-energy Σ, long-wavelength optical phonons can decay into two or more acoustic phonons. This leads to the observed shifts and broadenings. An *ab initio* calculation summing over all possible decay paths in the Brillouin zone has been performed by Debernardi [64, 65]. Empirically, we can use a Bose–Einstein expression (10) to describe the redshifts and broadenings, as shown by the solid lines in Figures 13 and 14.

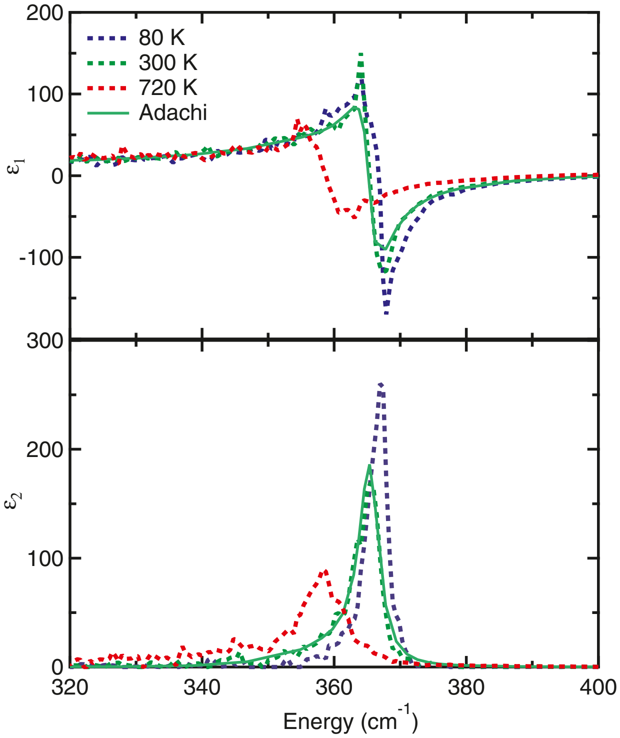

Figure 12: Temperature dependence of the dielectric function of GaP in the region of lattice absorption (dashed) in comparison with the literature (solid). Reprinted from ref. [28] with the permission of AIP Publishing.

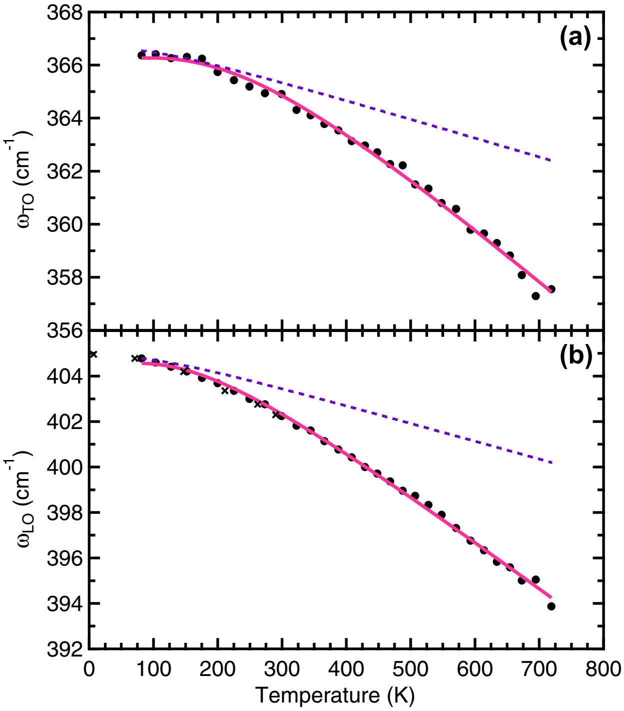

Figure 13: Temperature dependence of (a) transverse and (b) longitudinal optical phonon energies of GaP (·) in comparison to a Bose–Einstein model given by Eq. (10) (solid). The thermal expansion contribution from Eq. (4) is shown by the dashed line. Raman shifts (×) from ref. [63] are shown for comparison. See ref. [28] for details.

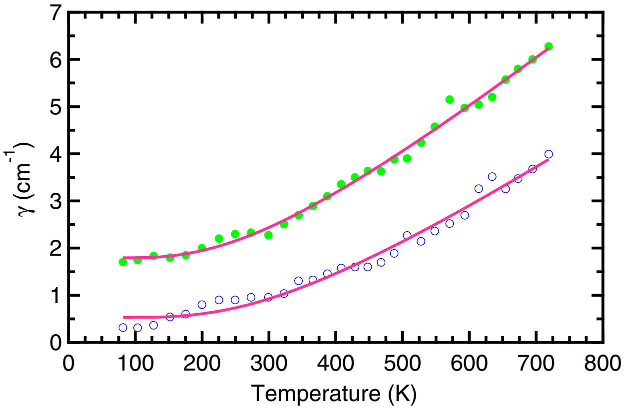

Figure 14: Broadenings of the transverse (·) and longitudinal (∘) optical phonons in GaP as a function of temperature. The lines show a fit with Eq. (10). Data from ref. [28].

6 Temperature dependence of the Drude response

The temperature dependence of the Drude contribution to the dielectric function in metals or doped semiconductors is determined by two parameters [7]: (1) the density of free carriers, which determines the unscreened plasma frequency $E_P{}^2 = \hbar^2 ne^2/\epsilon_0 m_0 m^*$, where ϵ_0 is the permittivity of vacuum, m_0 the free electron mass, and m^* an effective mass related to the curvature of the band, and (2) their scattering rate (proportional to the Drude broadening), which is related to the mobility. There may also be secondary effects, such as the temperature dependence of the effective masses [54]. Electron–phonon (or hole–phonon) scattering is often the dominating broadening mechanism in semiconductors [8] and metals [66].

In a metal like Au or Ni, the density of free carriers is nearly constant, given by the density of states at the Fermi level, which only depends weakly on temperature, for example through thermal expansion [66] or small shifts of band energies with temperature. The same is true for a doped semiconductor, where the carrier density is given by the density of activated donors or acceptors (doping density), as long as the temperature is low enough to ignore the intrinsic carriers discussed in Section 7. For metals and doped semiconductors, the temperature dependence of the Drude term is therefore dominated by the broadening parameter, which increases with temperature, similar to the broadening of band gaps and phonons shown in

Figures 8 and 14. This explains the increased resistivity (reduced conductivity) at high temperatures in such materials.

In a simple metal like Ag and Au, the Drude contribution to the dielectric function can be described with a single species of carriers, i.e., a single Drude term. At room temperature, the unscreened plasma energy of single-crystalline Au (Ag) is 8.5 (8.9) eV and the Drude broadening is 44 (18) meV [35, 66]. Temperature-dependent Drude parameters for different types of Ag films (single- and polycrystalline) were recently reported, derived from fits of ellipsometry data taken from 450 to 800 nm [66].

On the other hand, Drude already recognized in 1900 that two Drude terms were required to achieve a good description of the dielectric function of Ni [67–69]. This idea has not always been well received, but one might perhaps think of s- and d-electrons in transition metals (or electrons and holes in doped semiconductors), which might have different carrier densities and scattering rates. It is more common in the literature to describe the free carrier contribution of metals with a single Drude term, where the scattering rate depends on the photon energy [35, 70]. For this review, we prefer the approach with a finite number of Drude terms, each with a carrier density, effective mass, and scattering rate that are independent of photon energy.

To study the temperature dependence of the Drude parameters in Ni, we measured its dielectric function from 0.1 to 6.0 eV between 77 and 770 K. Since the resonance frequency of free carriers vanishes, because there is no restoring force, one introduces the optical conductivity

$$\sigma(\omega) = -i\epsilon_0\omega[\epsilon(\omega) - 1], \tag{12}$$

which removes the singularity of $\epsilon(\omega)$ at $\omega = 0$. Results for the real part σ_1, which corresponds to ϵ_2, are shown in Figure 15. The temperature dependence of the main peak at 4.8 eV has already been discussed in Section 4.

Both Drude scattering rates for Ni are shown in Figure 16. The scattering rate for d-electrons is very large (about 2.9 eV) and nearly independent of temperature. This should be expected, since the strongly localized d-electrons do not contribute much to the electrical conductivity. The scattering rate for s-electrons is much smaller (44 meV at room temperature) and shows a significant increase with temperature as expected for a metal. The slope of the scattering rate for s-electrons changes at the Curie temperature T_C, since the scattering mechanisms are different in the ferromagnetic and paramagnetic phases [71]. This kink is also observed in electrical conductivity measurements of Ni and Ni–Pt alloys [72]. In the paramagnetic phase above T_C, s-electrons with both spin states can scatter into d-bands, because both d-bands are only partially occupied. On the other hand, in the ferromagnetic state below T_C, one d-band is completely full. Therefore, s-electrons with spin up can scatter into the d-bands, while those with spin down cannot. This reduces the scattering rate of s-electrons very significantly in the ferromagnetic phase [71].

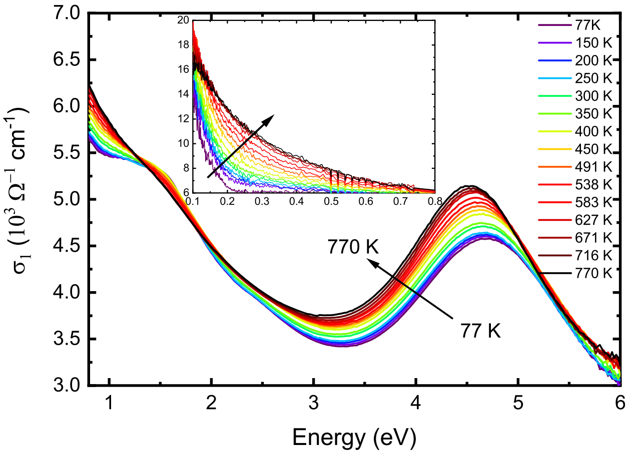

Figure 15: Real part of the optical conductivity of Ni from 0.1 to 6.0 eV between 77 and 770 K. Data from ref. [62].

The squares of the plasma frequencies ${E_P}^2$ for s- and d-electrons in Ni, which are determined by the ratios of the carrier density to the effective mass, also vary somewhat with temperature, but this is difficult to quantify, because the two plasma frequencies are correlated as fitting parameters in the Drude–Lorentz model used to fit the data shown in Figure 15. We can only state that ${E_P}^2$ equals

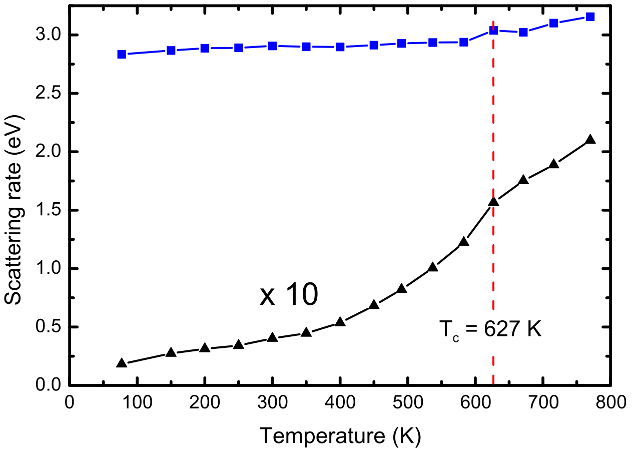

Figure 16: Temperature dependence of the Drude scattering rate for s- (▲) and d-electrons (■) of Ni between 77 and 770 K, determined from fitting the dielectric function. The Curie temperature T_C is shown by the vertical dashed line. Reprinted from ref. [62] with the permission of AIP Publishing.

23 ± 1 eV^2 for the s-electrons and ranges from about 140 eV^2 at low temperatures to 155 eV^2 at high temperatures for the d-electrons. It is helpful to know that $\hbar^2 e^2/\epsilon_0 m_0 = 1.379 \times 10^{-21}$ cm^3 eV^2. For an effective mass $m^* = 3$ for d-electrons, this plasma frequency corresponds to a free carrier density of about 3×10^{23} cm^{-3}. This means that 3.6 d-electrons per atom are near the Fermi level and can participate in electronic transport, an order of magnitude higher than what has been reported [73]. For s-electrons, we find a carrier concentration of 0.25 electrons per atom, which is reasonable [73]. Because of the uncertainty of the effective masses and their variation across the Brillouin zone [74], these carrier densities should only be considered rough estimates.

Another good example for the temperature dependence of the Drude response in complex metal oxides at very long wavelengths is $La_{2-x}Sr_xCuO_4$ [26].

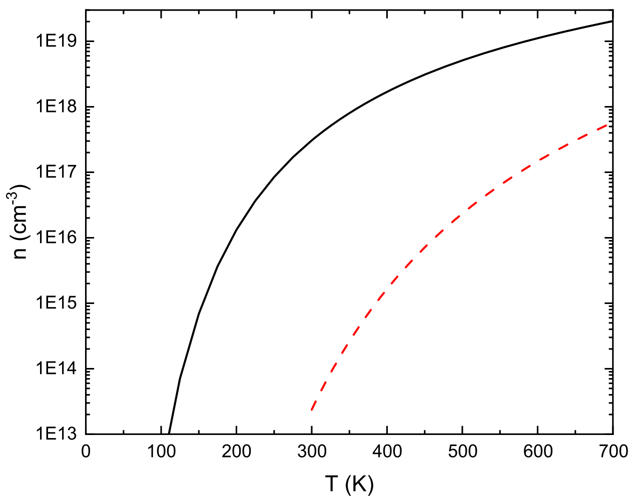

Figure 17: Carrier density of intrinsic InSb (solid) and Ge (dashed) as a function of temperature.

7 Temperature-dependent intrinsic carrier concentrations

In an intrinsic semiconductor (without dopants), the free carrier density is a strong function of temperature, through thermal excitation of electrons across the gap into the conduction band, given by [75, 76]

$$n = p = 2\left(\frac{km_0}{2\pi\hbar^2}\right)^{\frac{3}{2}}(m_e m_h)^{\frac{3}{4}} T^{\frac{3}{2}} \exp\left(-\frac{E_0}{2kT}\right) \qquad (13)$$

for a direct semiconductor with a single conduction band valley, such as InSb, see Figure 17. m_e and m_h are the density-of-states effective masses for electrons and holes, respectively. The prefactor equals 4.84×10^{15} cm^{-3}K$^{-3/2}$. Indirect materials like Ge have a more complex conduction band structure and several minima need to be considered [54]. Because of the smaller band gap of InSb compared to Ge, the intrinsic carrier concentration of InSb is much higher.

Following Eq. (13), even pure semiconductors should display a Drude contribution to the dielectric function at sufficiently high temperatures. We are not aware of such results for any semiconductor, but narrow-gap compounds such as InSb or InAs would be interesting candidates.

To illustrate this point, we show preliminary results for the temperature dependence of the energies and broadenings of the direct band gap of InSb in Figure 18 [77]. The mid-infrared pseudo-dielectric function of InSb was measured from 80 to 700 K with 16 cm^{-1} resolution in a UHV cryostat with diamond windows and corrected for a 2.5 nm thick native oxide with a constant $\epsilon = 3.8$. The resulting dielectric function of InSb was fitted from 500 to 5000 cm^{-1} with a parametric oscillator model similar to ref. [27]. The parameters in this model were the energy E_0, broadening Γ, and amplitude of the direct band gap and poles in the IR and UV outside the measured spectral range.

Below room temperature, the band gap E_0 follows Eq. (10) with reasonable parameters. Above room temperature, the data deviate from the model (dotted line). Between 300 and 600 K, E_0 is nearly constant and then even increases at the highest temperature. Our InSb sample melted at a thermocouple temperature of 750 K, just below the reported melting point of InSb of 800 K. Close to the

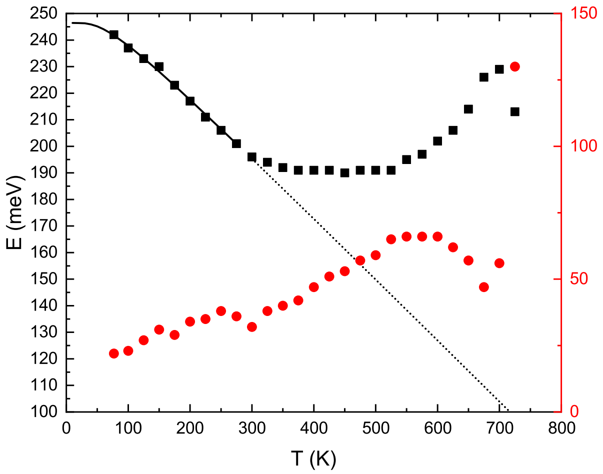

Figure 18: Temperature dependence of the energies E (■) and broadenings Γ (•) of the direct band gap of InSb. The lines show a Bose–Einstein fit to Eq. (10) with parameters $E_0 = 267$ meV, $E_b = 20.2$ meV, and $\Omega/k = 175$ K. Data from ref. [77].

melting point, both E_0 and Γ show an unexpected (anharmonic) behavior. We believe that thermally activated electron-hole pairs cause a blueshift of the band gap due a thermal Burstein–Moss shift [78]. This needs to be confirmed with detailed calculations.

8 Phase transitions in complex metal oxides

The literature contains many reports on the temperature dependence of the optical conductivity of materials, especially related to magnetic phase transitions, insulator to metal (Mott) transitions, and the superconducting transition of cuprates. Such results were usually obtained by near normal incidence reflectance followed by Kramers–Kronig transform [79]. In a reflectance measurement, the infrared beam can easily be focused on a small sample, while ellipsometry usually requires a much larger sample size. Therefore, ellipsometry studies of phase transitions are rare, since the size of single-crystal metal oxides is often quite small. On the other hand, ellipsometry directly measures the dielectric function of materials (at least in the absence of surface layers) and is not affected by the errors of a Kramers–Kronig transformation. Furthermore, infrared reflectance measurements can usually be carried out at lower photon energies than those accessible with commercial infrared ellipsometers. It can be useful to combine reflectance and ellipsometry measurements to obtain the dielectric function over a broad spectral range. Such an analysis has been performed to investigate the temperature dependence of the optical conductivity of nickelates [80].

As an example, the temperature dependence of the optical conductivity of a $NdNiO_3$ thin layer grown on $SrTiO_3$ is shown in Figure 19. Between 0.5 and 6.0 eV, the letters indicate several interband optical transitions between different molecular orbitals. In the mid-infrared range (0.02–0.08 eV), several sharp lattice absorption peaks can be seen. At even lower energies, the optical spectra are dominated by the Drude response. At temperatures below 100 K, the conductivity vanishes at low energies, indicating that the oxide is an insulator. Above 100 K, the optical conductivity is high at low energies and displays a clear Drude response indicating metallic character of the $NdNiO_3$. The insulator-to-metal transition occurs at about 100 K. The metallic response at the higher temperatures leads to a large broadening of the interband transitions A′ and B. The inset shows the temperature dependence of the plasma frequency, calculated from the optical sum rule [6] with different cut-off energies Ω. In the insulating regime below 100 K, the plasma frequency is low. It rises sharply at the transition temperature and then decreases gradually with increasing temperature. See ref. [80] for more detail.

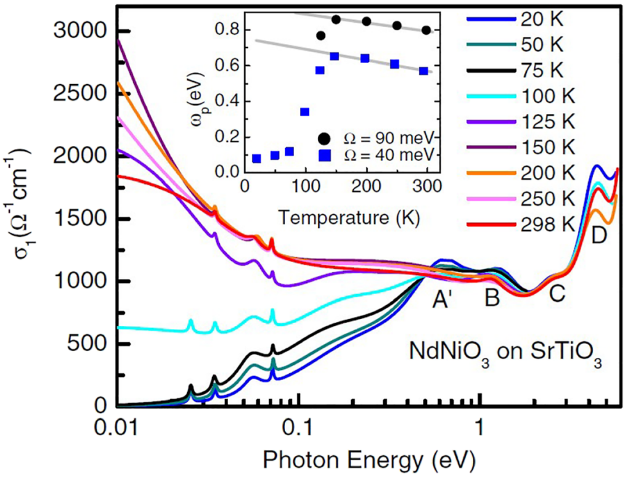

Figure 19: Temperature dependence of the optical conductivity of $NdNiO_3$ on $SrTiO_3$. The letters indicate interband optical transitions between different orbitals. The inset shows the temperature dependence of the plasma frequency. Note that only data above 60 meV were obtained by ellipsometry, while far-infrared data were derived from infrared reflectance. Reprinted with permission from ref. [80]. Copyright 2011 by the American Physical Society.

9 Phase-change materials

It is well known that the dielectric function of amorphous materials is very different from single- or poly-crystalline materials of the same composition. Crystalline materials show sharp critical points known as van Hove singularities, where unfilled and filled electron bands run parallel in the Brillouine zone, see Figure 9 [12, 29, 50]. Amorphous materials, on the other hand, show a single broad peak in the dielectric function, which can usually be described with a Tauc–Lorentz oscillator [1]. Silicon is a good example, which has been studied extensively in the amorphous state and after annealing at various temperatures [81, 82]. It is possible to determine the adiabatic amorphous to crystalline transition temperature by heating the sample in a UHV cryostat while performing spectroscopic ellipsometry measurements at preselected temperature intervals.

As an example, we show the temperature dependence of the dielectric function of carbon-doped $Ge_2Sb_2Te_5$ (GST) alloys [83] in Figure 20. Such GST alloys are commonly used in optical recording and non-volatile semiconductor

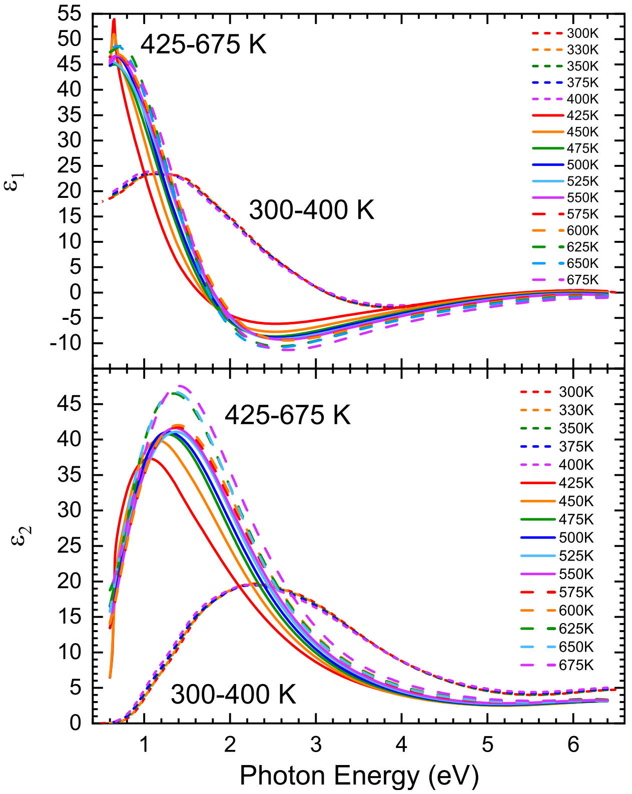

Figure 20: Temperature dependence of the dielectric function of $Ge_2Sb_2Te_5$:C. Data from ref. [83].

memories or as tunable infrared optical filters [84]. They are crystalline at high temperatures and remain crystalline at room temperature if cooled slowly. Rapid cooling, however, leads to an amorphous state with a very different dielectric function.

For this work, 750 nm of GST:C were deposited on Si wafers covered with a 400 nm thick thermal oxide. As deposited, the layers are amorphous with a band gap of about 1 eV, which is indicated by sharp interference fringes in the ellipsometric angles below the gap (not shown). The alloys remain amorphous when heated to 400 K and display a very broad peak of ϵ_2 centered on 2.5 eV, nearly independent of temperature. At higher temperatures (425–675 K), the onset of absorption decreases below 0.5 eV, the interference fringes disappear, and the main absorption peak is much narrower, indicating a crystalline phase. When heated from 425 to 675 K, the absorption peak blueshifts from 1.0 to 1.5 eV and its integrated intensity increases. This is unusual, since peaks in ϵ_2 usually redshift with increasing temperature, see Figure 15. At even higher temperatures (above 700 K), the layer evaporates and only the thermal oxide remains on the wafer. This example demonstrates the power of *in situ* ellipsometry for thermal process monitoring.

10 Summary

Temperature-dependent spectroscopic ellipsometry from the infrared to the ultraviolet spectral region inside a UHV cryostat is a powerful method to investigate the interactions of electronic and vibrational states with other quasiparticles. The required experimental techniques were described in detail and selected examples were presented.

Acknowledgement: The authors acknowledge the contributions of many undergraduate students at New Mexico State University who have contributed to this work over the past decade, as cited in the references. We are also grateful to our colleagues who suggested topics and references to include in this review.

Author contributions: All the authors have accepted responsibility for the entire content of this submitted manuscript and approved submission.

Research funding: This work was supported by the National Science Foundation (DMR-1104934 and DMR-1505172), the Air Force Office of Scientific Research (FA9550-13-1-0022 and FA9550-20-1-0135), and the Army Research Office (W911NF-16-1-0492).

Conflict of interest statement: The authors declare no conflicts of interest regarding this article. References to commercially available products are not to be considered an endorsement. Similar products may be available from other suppliers or can be built by those skilled in the art.

References

[1] H. Fujiwara, *Spectroscopic Ellipsometry*, Chichester, Wiley, 2007.

[2] D. E. Aspnes, “Spectroscopic ellipsometry—a perspective,” *J. Vac. Sci. Technol, A*, vol. 31, p. 058502, 2013.

[3] H. G. Tompkins and J. N. Hilifiker, *Spectroscopic Ellipsometry: Practical Application to Thin-Film Characterization*, New York, Momentum, 2016.

[4] S. Zollner, “Spectroscopic ellipsometry for inline process control in the semiconductor industry,” in *Ellipsometry at the Nanoscale*, M. Losurdo and K. Hingerl, Eds., Heidelberg, Springer, 2013, pp. 607–627.

[5] M. Fox, *Optical Properties of Solids*, Oxford, Oxford University Press, 2010.

[6] F. Wooten, *Optical Properties of Solids*, New York, Academic, 1972.

[7] S. Zollner, P. P. Paradis, F. Abadizaman, and N. S. Samarasingha, “Drude and Kukharskii mobility of doped semiconductors extracted from Fourier transform infrared ellipsometry spectra,” *J. Vac. Sci. Technol. B*, vol. 37, p. 012904, 2019.

[8] M. Cardona and S. Gopalan, “Temperature dependence of the band structure of semiconductors: electron-phonon

interaction," in *Progress in Electron Properties of Solids. Physics and Chemistry of Materials with Low-Dimensional Structures*, vol. 10, E. Doni, R. Girlanda, and G. Pastori Parravicini, Eds., Dordrecht, Springer, 1989, pp. 51–64.

[9] J. Menéndez and M. Cardona, "Temperature dependence of the first-order Raman scattering by phonons in Si, Ge, and α-Sn: anharmonic effects," *Phys. Rev. B*, vol. 29, pp. 2051–2059, 1984.

[10] S. Gopalan, P. Lautenschlager, and M. Cardona, "Temperature dependence of the shifts and broadenings of the critical points in GaAs," *Phys. Rev. B*, vol. 35, pp. 5577–5584, 1987.

[11] Linkam Scientific Instruments, Tadworth, United Kingdom. Available at: https://www.linkam.co.uk/.

[12] J. Šik, J. Hora, and J. Humlíček, "Optical functions of silicon at high temperatures," *J. Appl. Phys.*, vol. 84, pp. 6291–6298, 1998.

[13] R. Schmidt-Grund, H. Krauß, C. Kranert, M. Bonholzer, and M. Grundmann, "Temperature dependence of the dielectric function in the spectral range (0.5–8.5) eV of an InO thin film," *Appl. Phys. Lett.*, vol. 105, p. 111906, 2014.

[14] C. Sturm, R. Schmidt-Grund, V. Zviagin, and M. Grundmann, "Temperature dependence of the dielectric tensor of monoclinic GaO single crystals in the spectral range 1.0–8.5 eV," *Appl. Phys. Lett.*, vol. 111, p. 082102, 2017.

[15] E. Krüger, V. Zviagin, C. Yang, C. Sturm, R. Schmidt-Grund, and M. Grundmann, "Temperature dependence of the dielectric function of thin film CuI in the spectral range (0.6–8.3) eV," *Appl. Phys. Lett.*, vol. 113, p. 172102, 2018.

[16] Lakeshore Cryotronics, Inc, Woburn, MA, USA. Available at: https://www.lakeshore.com/products/product-detail/janis/st-400-uhv-cryostat.

[17] A. A. Studna, D. E. Aspnes, L. T. Florez, B. J. Wilkens, J. P. Harbison, and R. E. Ryan, "Low-retardance fused-quartz window for real-time optical applications in ultrahigh vacuum," *J. Vac. Sci. Technol, A*, vol. 7, pp. 3291–3294, 1989.

[18] I. Bomco and M. A. Gloucester, USA. Available at: http://www.bomco.com/products/.

[19] F. Abadizaman, "Optical characterization of Ni using spectroscopic ellipsometry at temperatures from 80 K to 780 K," Ph.D. thesis, New Mexico State University, 2020.

[20] Diamond Materials GmbH, Freiburg, Germany. Available at: https://www.diamond-materials.com/unsere-produkte/strahlungsfenster/uhv-vakuumfenster/.

[21] Shibuya Optical Co., Ltd., Wako-shi, Saitama, Japan. Available at: https://www.shibuya-opt.co.jp/eng/uhv_window.html.

[22] Korth Kristalle GmbH, Altenholz, Germany. Available at: https://www.korth.de.

[23] Crystran Ltd, Poole, UK. Available at: https://www.www.crystran.co.uk.

[24] Thorlabs Inc, Newton, NJ, USA. Available at: https://www.thorlabs.com.

[25] A. B. Sushkov and E. A. Tishchenko, "Low-temperature far-infrared ellipsometry of convergent beam," *Int. J. Infrared Milli.*, vol. 14, pp. 2555–2568, 1993.

[26] R. Henn, C. Bernhard, A. Wittlin, M. Cardona, and S. Uchida, "Far-infrared ellipsometry using synchrotron radiation: the out-of-plane response of LaSr$_x$CuO," *Thin Solid Films*, vols 313-314, pp. 642–648, 1998.

[27] C. Emminger, F. Abadizaman, N. S. Samarasingha, T. E. Tiwald, and S. Zollner, "Temperature dependent dielectric function and direct bandgap of Ge," *J. Vac. Sci. Technol. B*, vol. 38, p. 012202, 2020.

[28] N. S. Samarasingha and S. Zollner, "Temperature dependence of the optical phonon reflection band in GaP," *J. Vac. Sci. Technol. B*, vol. 39, p. 052201, 2021.

[29] D. E. Aspnes and A. A. Studna, "Dielectric functions and optical parameters of Si, Ge, GaP, GaAs, GaSb, InP, InAs, and InSb from 1.5 to 6.0 eV," *Phys. Rev. B*, vol. 27, pp. 985–1009, 1983.

[30] S. Choi, J. Zúñiga-Pérez, V. Muñoz-Sanjosé, A. G. Norman, C. L. Perkins, and D. H. Levi, "Complex dielectric function and refractive index spectra of epitaxial CdO thin film grown on r-plane sapphire from 0.74 to 6.45 eV," *J. Vac. Sci. Technol. B*, vol. 28, pp. 1120–1124, 2010.

[31] T. N. Nunley, T. I. Willett-Gies, J. A. Cooke, et al., "Optical constants, band gap, and infrared-active phonons of (LaAlO)(SrAlTaO) (LSAT) from spectroscopic ellipsometry," *J. Vac. Sci. Technol., A*, vol. 34, p. 051507, 2016.

[32] L. S. Abdallah, T. M. Tawalbeh, I. V. Vasiliev, et al., "Optical conductivity of NiPt$_x$ alloys (0x0.25) from 0.76 to 6.6 eV," *AIP Adv.*, vol. 4, p. 017102, 2014.

[33] G. E. Jellison and B. C. Sales, "Determination of the optical functions of transparent glasses by using spectroscopic ellipsometry," *Appl. Opt.*, vol. 30, pp. 4310–4315, 1991.

[34] T. N. Nunley, N. S. Fernando, N. Samarasingha, et al., "Optical constants of germanium and thermally grown germanium dioxide from 0.5 to 6.6 eV via a multi-sample ellipsometry investigation," *J. Vac. Sci. Technol. B*, vol. 34, p. 061205, 2016.

[35] F. Abadizaman and S. Zollner, "Optical constants of polycrystalline Ni from 0.06 to 6.0 eV at 300 K," *J. Vac. Sci. Technol. B*, vol. 37, p. 062920, 2019.

[36] S. Zollner, T. N. Nunley, D. P. Trujillo, L. G. Pineda, and L. S. Abdallah, "Temperature-dependent dielectric function of Nickel," *Appl. Surf. Sci.*, vol. 421, pp. 913–916, 2017.

[37] G. P. Pells, "Measurement of the optical properties of alloys in ultra-high vacuum," *J. Sci. Instrum.*, vol. 44, pp. 997–1000, 1967.

[38] M. Shiga and G. P. Pells, "The optical properties of nickel above and below the Curie temperature," *J. Phys. C Solid State Phys.*, vol. 2, pp. 1847–1856, 1969.

[39] G. P. Pells and M. Shiga, "The optical properties of copper and gold as a function of temperature," *J. Phys. C Solid State Phys.*, vol. 2, pp. 1835–1846, 1969.

[40] L. Viña, S. Logothetidis, and M. Cardona, "Temperature dependence of the dielectric function of germanium," *Phys. Rev. B*, vol. 30, pp. 1979–1991, 1984.

[41] S. Zollner, M. Garriga, J. Humlíček, S. Gopalan, and M. Cardona, "Temperature dependence of the dielectric function and the interband critical-point parameters of GaSb," *Phys. Rev. B*, vol. 43, pp. 4349–4360, 1991.

[42] S. Zollner, M. Cardona, and S. Gopalan, "Isotope and temperature shifts of direct and indirect band gaps in diamond-type semiconductors," *Phys. Rev. B*, vol. 45, pp. 3376–3385, 1992.

[43] S. Zollner, M. Garriga, J. Kircher, J. Humlíček, M. Cardona, and G. Neuhold, "Temperature dependence of the dielectric function and the interband critical-point parameters of GaP," *Phys. Rev. B*, vol. 48, pp. 7915–7929, 1993.

[44] P. B. Allen and V. Heine, "Theory of the temperature dependence of electronic band structures," *J. Phys. C Solid State Phys.*, vol. 9, pp. 2305–2312, 1976.

[45] M. Born and E. Wolf, *Principles of Optics*, 6th ed. Oxford, Pergamon, 1980, pp. 177–180.

[46] D. Tentori and J. R. Lerma, "Refractometry by minimum deviation: accuracy analysis," *Opt. Eng.*, vol. 29, pp. 160–168, 1990.

[47] J. H. Burnett, E. C. Benck, S. G. Kaplan, E. Stover, and A. Phenis, "Index of refraction of germanium," *Appl. Opt.*, vol. 13, pp. 3985–3991, 2020.

[48] K. Vedam, J. L. Kirk, and B. N. N. Achar, "Piezo- and thermo-optic behavior of spinel (MgAlO)," *J. Solid State Chem.*, vol. 12, pp. 213–218, 1975.

[49] R. Gupta and S. G. Kaplan, "High accuracy ultraviolet index of refraction measurements using a fourier transform spectrometer," *J. Res. Natl. Inst. Stand. Technol.*, vol. 108, pp. 429–437, 2003.

[50] P. Y. Yu and M. Cardona, *Fundamentals of Semiconductors*, Berlin, Springer, 2010.

[51] C. J. Zollner, T. I. Willett-Gies, S. Zollner, and S. Choi, "Infrared to vacuum-ultraviolet ellipsometry studies of spinel (MgAlO)," *Thin Solid Films*, vol. 571, pp. 689–694, 2014.

[52] C. M. Nelson, M. Spies, L. S. Abdallah, S. Zollner, Y. Xu, and H. Luo, "Dielectric function of LaAlO from 0.8 to 6 eV between 77 and 700 K," *J. Vac. Sci. Technol., A*, vol. 30, p. 061404, 2012.

[53] R. Schmidt-Grund, N. Ashkenov, M. M. Schubert, et al., "Temperature-dependence of the refractive index and the optical transitions at the fundamental band-gap of ZnO," *AIP Conf. Proc.*, vol. 893, pp. 271–272, 2007.

[54] C. Emminger, N. S. Samarasingha, M. Rivero Arias, F. Abadizaman, J. Menéndez, and S. Zollner, "Excitonic effects at the temperature-dependent direct band gap of Ge," *J. Appl. Phys.*, vol. 131, p. 165701, 2022.

[55] A. Mock, J. VanDerslice, R. Korlacki, J. A. Woollam, and M. Schubert, "Elevated temperature dependence of the anisotropic visible-to-ultraviolet dielectric function of monoclinic β-GaO," *Appl. Phys. Lett.*, vol. 112, p. 041905, 2018.

[56] H.-W. Chen, C.-Y. Huang, G.-J. Shu, and H.-L. Liu, "Temperature-dependent optical properties of CuFeO through the structural phase transition," *RSC Adv.*, vol. 11, pp. 40173–40181, 2021.

[57] M.-J. Pan and C. A. Randall, "A brief introduction to ceramic capacitors," *IEEE Electr. Insul. Mag.*, vol. 26, pp. 44–50, 2010.

[58] D. E. Aspnes, "Third-derivative modulation spectroscopy with low-field electroreflectance," *Surf. Sci.*, vol. 37, pp. 418–442, 1973.

[59] D. E. Aspnes, "Modulation spectroscopy/elecgtric field effects on the dielectric function of semiconductors," in *Handbook on Semiconductors*, vol. 2, M. Balkanski, Ed., Amsterdam, North Holland, 1980, p. 109.

[60] C. Tanguy, "Analytical expression of the complex dielectric function for the Hulthén potential," *Phys. Rev. B*, vol. 60, pp. 10660–10663, 1999.

[61] J. W. Garland, C. Kim, H. Abad, and P. M. Raccah, "Determination of accurate critical-point energies and linewidths from optical data," *Phys. Rev. B*, vol. 41, pp. 7602–7610, 1990.

[62] F. Abadizaman, J. Love, and S. Zollner, "Optical constants of single-crystalline Ni (100) from 77 K to 770 K from ellipsometry measurements," *J. Vac. Sci. Technol, A*, vol. 40, p. 033202, 2022.

[63] B. K. Bairamov, D. A. Parshin, V. V. Toporov, and S. B. Ubaidullaev, "High-resolution study of the scattering of light by longitudinal optical phonons in a GaP crystal", *Pis'ma zh. Tekh. Fiz.*, vol. 5, p. 1116, 1979. (Sov. Tech. Phys. Lett., vol. 5, pp. 466–467, 1979).

[64] A. Debernardi, "Phonon linewidth in III-V semiconductors from density-functional perturbation theory," *Phys. Rev. B*, vol. 57, pp. 12847–12858, 1998.

[65] A. Debernardi, "Anharmonic effects in the phonons of III-V semiconductors: first principles calculations," *Solid State Commun.*, vol. 113, pp. 1–10, 2000.

[66] S. V. Jayanti, J. H. Park, A. Dejneka, et al., "Low-temperature enhancement of plasmonic performance in silver films," *Opt. Mater. Express*, vol. 5, pp. 1147–1155, 2015.

[67] P. Drude, "Zur ionentheorie der Metalle," *Phys. Z.*, vol. 1, pp. 161–165, 1900.

[68] S. Roberts, "Interpretation of the optical properties of metal surfaces," *Phys. Rev.*, vol. 100, pp. 1667–1671, 1955.

[69] S. Roberts, "Optical properties of nickel and tungsten and their interpretation according to Drude's formula," *Phys. Rev.*, vol. 114, pp. 104–115, 1959.

[70] P. E. Sulewski, A. J. Sievers, M. B. Maple, M. S. Torikachvili, J. L. Smith, and Z. Fisk, "Far-infrared absorptivity of UPt," *Phys. Rev. B*, vol. 38, pp. 5338–5352, 1988.

[71] N. F. Mott, "Electrons in transition metals," *Adv. Phys.*, vol. 13, pp. 325–422, 1964.

[72] H. Litschel and I. Pop, "Temperature dependence of the electrical resistivity of the nickel-platinum alloy system," *J. Phys. Chem. Solid.*, vol. 46, pp. 1421–1425, 1985.

[73] H. Ehrenreich, H. R. Philipp, and D. J. Olechna, "Optical properties and fermi surface of nickel," *Phys. Rev.*, vol. 131, pp. 2469–2477, 1963.

[74] C. S. Wang and J. Callaway, "Band structure of nickel: spin-orbit coupling, the fermi surface, and the optical conductivity," *Phys. Rev. B*, vol. 9, pp. 4897–4907, 1974.

[75] S. M. Sze, *Physics of Semiconductor Devices*, New York, Wiley, 1981.

[76] C. Kittel, *Introduction to Solid State Physics*, New York, Wiley, 2005.

[77] M. Rivero Arias, C. M. Zamarripa, J. R. Love, C. Emminger, and S. Zollner, "Temperature dependence of the mid-infrared dielectric function of InSb from 80 to 800 K," (unpublished).

[78] M. Grundmann, *The Physics of Semiconductors*, Cham, Springer, 2006.

[79] Y. Tokura, Y. Okimoto, S. Yamaguchi, H. Taniguchi, T. Kimura, and H. Takagi, "Thermally induced insulator-metal transition in LaCoO: a view based on the Mott transition," *Phys. Rev. B*, vol. 58, pp. R1699–R1792, 1978.

[80] M. K. Stewart, J. Liu, M. Kareev, J. Chakhalian, and D. N. Basov, "Mott physics near the insulator-to-metal transition in NdNiO," *Phys. Rev. Lett.*, vol. 107, p. 176401, 2011.

[81] M. Fried, T. Lohner, W. A. M. Aarnink, L. J. Hanekamp, and A. van Silfhout, "Determination of complex dielectric functions of ion implanted and implanted-annealed amorphous silicon by spectroscopic ellipsometry," *Appl. Phys. Lett.*, vol. 71, pp. 5260–5262, 1991.

[82] S. Zollner, R. Liu, J. Christiansen, et al., "Raman and spectroscopic ellipsometry studies of P-doped poly-Si," in *Amorphous and Microcrystalline Silicon Technology-1998*, R. Schropp, H. M. Branz, M. Hack, I. Shimizu, and S. Wagner, Eds., Pittsburgh, Materials Research Society, 1998, pp. 957–962.

[83] C. M. Zamarripa, N. Samarasingha, F. Abadizaman, R. A. Carrasco, and S. Zollner, *Temperature-Dependent*

Ellipsometry and Thermal Stability of GeSbTe:C Phase Change Memory Alloys, Long Beach, CA, AVS 65th International Symposium and Exhibition, 2018, (unpublished).

[84] J. Orava, T. Wágner, J. Šik, J. Přikryl, M. Frumar, and L. Beneš, "Optical properties and phase change transition in GeSbTe flash evaporated thin films studied by temperature dependent spectroscopic ellipsometry," *J. Appl. Phys.*, vol. 104, p. 043523, 2008.

Bionotes

Stefan Zollner
Department of Physics, New Mexico State University, Las Cruces, NM, USA
zollner@nmsu.edu
https://orcid.org/0000-0001-7752-7941

Stefan Zollner received his Ph.D. in physics in 1991 with a thesis on temperature-dependent spectroscopic ellipsometry at the Max–Planck-Institute for Solid State Research in Stuttgart, Germany. After a postdoctoral year at the IBM Research Division in Yorktown Heights, NY, he accepted a faculty position in physics at Iowa State University in Ames, IA, with a joint appointment at Ames Laboratory (US-DOE). He joined the Motorola Semiconductor Products Sector in Mesa, AZ, in 1997 and subsequently worked in semiconductor metrology and process integration for Freescale and IBM in Tempe, AZ, Austin, TX, and East Fishkill, NY. Since 2010, he has been a professor of physics and the head of the physics department at New Mexico State University in Las Cruces, NM. He is a fellow of the American Physical Society and the American Vacuum Society and an IEEE Senior Member. His professional service includes the chair-line of the Forum on Industrial and Applied Physics and the Executive Board of the American Physical Society.

Farzin Abadizaman
Department of Physics, New Mexico State University, Las Cruces, NM, USA
abadizaman@physics.muni.cz

Farzin Abadizaman received his MS (Spring 2018) and Ph.D. in Physics (Fall 2020) from New Mexico State University. His dissertation focused on optical properties of Ni as a function of temperature using spectroscopic ellipsometry. His main focus was on the optical characterization of the magnetic phase change in Ni. Farzin currently works as a postdoc at Masaryk University in the Czech Republic and conducts research on the phase transitions in complex metal oxides at the Central European Institute of Technology (CEITEC).

Carola Emminger
Department of Physics, New Mexico State University, Las Cruces, NM, USA
carola.emminger@uni-leipzig.de

Carola Emminger received a PhD in Physics from New Mexico State University in May 2022 for her work on the temperature dependence of the optical constants of semiconductors obtained from spectroscopic ellipsometry, with a focus on the direct band gap of Ge, as well as the computational analysis of time-resolved optical constants measured with femtosecond pump-probe spectroscopic ellipsometry at ELI Beamlines (Czech Republic). Currently, she is employed as a postdoc at Leipzig University and Humboldt University of Berlin, where she is working in the project FAIRmat, one of the flagships of the German National Research-Data Infrastructure.

Nuwanjula Samarasingha
Department of Physics, New Mexico State University, Las Cruces, NM, USA
nuwanjula-s@novami.com

Nuwanjula Samarasingha received her MS (Spring 2018) and Ph.D. in Physics (Fall 2021) from New Mexico State University. Her dissertation focused on optical and structural characterization of compound semiconductor materials using spectroscopic ellipsometry (UV, FTIR), X-ray diffraction (XRD), X-ray reflectivity (XRR), and atomic force microscopy (AFM). She mainly worked on the thickness-dependent optical properties of II-VI compound semiconductor thin films from the mid-infrared to the vacuum-ultraviolet and the temperature dependence of optical phonon reflection bands in III-V compound semiconductors. Nuwanjula currently works as an application engineer at Nova Process Insight in Oregon.